COMMUNICATIONS

Picoliter ¹H NMR Spectroscopy

Kevin R. Minard and Robert A. Wind

Pacific Northwest National Laboratory, P.O. Box 999, Richland, WA 99352

In this study, a 267-μm-diameter solenoid transceiver is used to acquire localized ¹H NMR spectra and the measured signal-to-noise ratio (SNR) at 500 MHz is shown to be within 20–30% of theoretical limits formulated by considering only its resistive losses. This is illustrated using a 100-μm-diameter globule of triacylglycerols ($\sim$900 mM) that may be an oocyte precursor in young *Xenopus laevis* frogs and a water sample containing choline at a concentration often found in live mammalian cells ($\sim$33 mM). In chemical shift imaging (CSI) experiments performed using a few thousand total scans, the choline methyl line is shown to have an acceptable SNR in resolved volume elements containing only 50 pL of sample, and localized spectra are resolved from just 5 pL in the *Xenopus* globule. These findings demonstrate the feasibility of performing ¹H NMR on picoliter-scale sample volumes in biological cells and tissues and illustrate how the achieved SNR in spectroscopic images can be predicted with reasonable accuracy at microscopic spatial resolutions. © 2002 Elsevier Science (USA)

Key Words: picoliter ¹H NMR; microscopy; CSI; SNR; microcoil.

INTRODUCTION

As the dimensions of a solenoidal receiver coil are reduced, the signal-to-noise ratio (SNR) achieved per unit sample volume increases in ¹H NMR (*1*). Recognition of this has led to the widespread use of small coils with sensitive volumes on the order of a microliter or less. In imaging applications, these so-called microcoils are routinely used to compensate for the loss of signal that inevitably occurs as spatial resolution is increased, and images of water with resolved volume elements as small as 0.2–2 pL have been acquired (*2–4*). In contrast, volumes no smaller than 5–10 nL have been used for detecting trace chemicals in ¹H NMR spectra—even though microcoils were also employed (*5–7*). Of course, in part, larger volumes are necessary since the concentration of chemically equivalent protons in detected compounds is often significantly lower than for bulk water. Nevertheless, if only resistive losses in a microcoil are considered, theory suggests that it should often be possible to detect the presence of trace substances in tens of picoliter volumes. Here, the theoretical basis for this is reviewed and

expected SNR performance is demonstrated at 500 MHz using a 267-μm-diameter solenoid and three-dimensional chemical shift imaging (3D-CSI). To establish relevance to cellular research, experiments are performed using biological tissue and a water sample containing choline at a concentration typically found in live cells.

THEORETICAL CONSIDERATIONS

In principle, CSI is well suited to acquiring localized ¹H NMR spectra from small sample volumes since it provides the highest possible SNR per unit measuring time when compared with other spectroscopic imaging methods (*8*). In the 3D spin-echo experiment illustrated in Fig. 1, the magnetization within a slice is excited and the time-dependent voltage induced across the receiver coil is spatially encoded using two orthogonal phase encoding gradients. A two-dimensional Fourier transform (FT) is then used to determine the contribution—$S(t)$—that arises from magnetization in different sample volumes throughout the selected slice (*9*). If the root mean square (RMS) noise in $S(t)$ is denoted by σ_t, then the time-domain signal-to-noise ratio (SNR$_t$) is defined here as the maximum signal amplitude at the time of the spin-echo $S(t = \text{TE})$ divided by twice the RMS noise—

$$\text{SNR}_t = S(t = \text{TE})/2\sigma_t. \quad [1]$$

In the following sections, the factors affecting the observed SNR are briefly reviewed by first calculating the strength of the localized, time-domain ¹H NMR signal $S(t)$, and then the RMS value of accompanying noise (σ_t). Results are then exploited to predict the signal-to-noise ratio in the frequency domain (SNR$_f$) after a third FT is used to generate data consisting of two spatial dimensions (in the plane of the selected slice) and a third that contains the chemical shift spectrum for each resolved volume element or voxel.

The Localized Time-Domain Signal S(t)

When the magnetization around any particular voxel is fairly uniform, its localized ¹H NMR signal $S(t)$ is mathematically
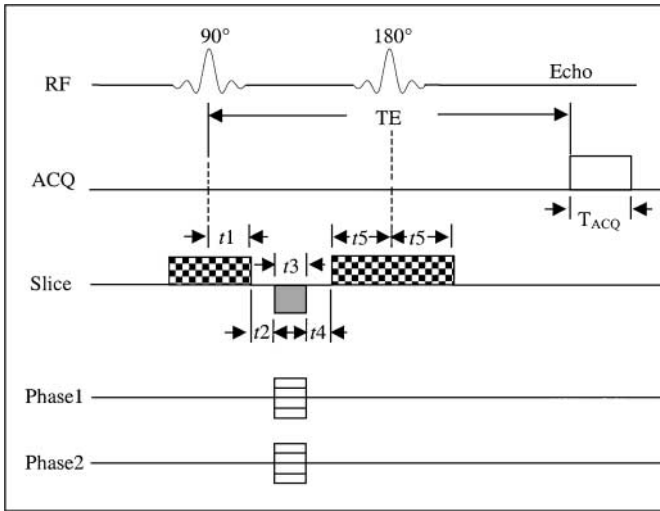
FIG. 1. Timing diagram for 3D-CSI. The pulse sequence produces a spin echo at time TE following the initial, slice-selective 90° excitation pulse. Data are collected during the second half of the spin echo for a total acquisition time T_{ACQ}. The various delays $t1$–$t5$ define the gradient waveform applied along the slice select axis. In practice, these are important for describing the severity of diffusion-induced signal losses (see Eqs. [5] and [6]) that occur when thin slices are employed. For any particular slice thickness, the checkered slice-select gradient pulses have an amplitude G_{slice}, and the amplitude of the solid slice-refocussing pulse is just $G_{slice}(t1/t3)$.

equivalent to the signal that would result if *only its* magnetization contributed to the induced voltage and data were coherently averaged during a fictitious CSI experiment performed without phasing encoding gradients (*10*). Exploiting this, together with the Principle of Reciprocity (*11–13*), then gives the following expression for the localized NMR signal, particularly when raw CSI data are collected in resonance with a phase-sensitive detector using N_{total} scans and the carrier frequency (ω_0) is removed:

$$S(t) = N_{total}\omega_0 M_{xy}(t)B_{xy}V_{voxel}. \qquad [2]$$

Here, $\omega_0 (=\gamma B_0)$ is the Larmor frequency determined by the proton gyromagnetic ratio ($\gamma = 2.675 \times 10^8 \text{ s}^{-1} \text{ T}^{-1}$) and the static magnetic field strength (B_0), $M_{xy}(t)$ represents the time-dependent amplitude of the transverse magnetization contained within the voxel of interest, V_{voxel} represents its volume (m^3), and B_{xy} denotes the amplitude of the transverse magnetic field produced per ampere at the voxel's location when a current oscillating at ω_0 flows through the receiver coil.

In high-frequency ^{1}H NMR, complex distortions in B_{xy} can arise from propagation delays introduced as current travels along the conducting wire (*13, 14*) and when dielectric standing waves are supported in the sample (*15, 16*). Fortunately, if a microcoil is employed, these are negligible and the radiofrequency (RF) magnetic field (B_{xy}) may be considered merely as an alternating version of the field produced by a dc current. In this so-called quasi-static limit, RF field strength inside the homogeneous re-

gion of a microcoil wound with n turns is described by the following expression (*17*):

$$B_{xy} = \frac{n\mu_0}{d_{coil}\sqrt{1 + (l_{coil}/d_{coil})^2}}. \qquad [3]$$

In this formula, μ_0 represents the magnetic permeability of free space ($4\pi \times 10^{-7}$ T m/A), l_{coil} denotes the coil's length, and d_{coil} represents its diameter—each of which is measured from wire-center to wire-center.

When the pulse sequence shown in Fig. 1 is repeated N_{total} times during CSI data collection, the sample's transverse magnetization $M_{xy}(t)$ quickly achieves a steady state that can be expressed in terms of the thermal equilibrium magnetization (M_0) and a loss factor β that describes the severity of T_1, T_2 and diffusion losses (*18, 19*):

$$M_{xy}(t) = M_0\beta(t). \qquad [4]$$

If the echo-time (TE) is much shorter than the repetition-time (TR) between successive acquisitions, β is described by the following formula when $\text{TE} \leq t \leq \text{TE} + T_{ACQ}$ (*18*):

$$\beta(t) = e^{-t/T_2}e^{-b_{slice}D}\{1 - e^{-TR/T_1}\}. \qquad [5]$$

In this expression, D represents the diffusion coefficient (m^2/s) for the molecule of interest, and b_{slice} (s/m^2) describes the sensitivity of the experiment to molecular diffusion along the slice select axis. Using a procedure outlined elsewhere (*18*), this so-called b-factor can be expressed in terms of the slice select gradient strength (G_{slice}, T/m) and the various timing parameters that define the gradient waveform shown in Fig. 1,

$$b_{slice} = \frac{1}{3}\gamma^2 G_{slice}^2\{t1^3 + t1^2(3t2 + t3) + 2t5^3\}. \qquad [6]$$

While diffusion losses are also induced by phase encoding gradients, these can be safely neglected since they are negligible compared to those incurred by slice selection (*20*).

Finally, the sample's thermal equilibrium magnetization (M_0) is given by (*18, 19*)

$$M_0 = N\gamma^2\hbar^2 I(I + 1)B_0/3 k_B T_s. \qquad [7]$$

Moreover, if a molecule's molar concentration (C) is known, then the spin density N for protons contributing to a particular chemical shift is conveniently calculated using Avogadro's number ($N_A = 6.02 \times 10^{23}$) and the number of chemically equivalent protons per molecule (n_s),

$$N = 1000 N_A C n_s. \qquad [8]$$

Other constants in Eq. [7] include the spin quantum number ($I = 1/2$ for protons), the sample's temperature (T_s, K), Planck's

constant divided by 2π ($\hbar = 1.05 \times 10^{-34}$ J s), and Boltzmann's constant ($k_B = 1.38 \times 10^{-23}$ J/K).

Time-Domain Noise

Previous analysis of NMR sensitivity in images created by Fourier reconstruction shows that the time-domain noise in the localized NMR signal is the incoherent average of noise introduced during each acquisition of the imaging experiment (*18*). When a microcoil with very short leads is employed, this arises primarily from the dissipation of electromagnetic energy in the coil itself, since sample losses decrease rapidly with coil size (*21*), and losses in the tuning capacitor can be made relatively small merely by winding a coil with many turns of thin wire (*22*). In this case, the RMS noise (σ_t) in the localized time-domain NMR signal $S(t)$ can be expressed by the well-known Nyquist formula,

$$\sigma_t = F' \sqrt{N_{total} 4 k_B T_{coil} R_{coil} \Delta f}. \qquad [9]$$

Here, R_{coil} represents the microcoil's ac resistance, T_{coil} represents its temperature (K), Δf is the receiver bandwidth (Hz), and F' is the *noise factor* of the preamplifier—which is easily related to its *noise figure* F (dB) ($F' = 10^{F/20}$ (*13*)).

Recent work shows that the ac resistance of a microcoil wound with a total length (l) of round copper wire having a diameter (d) greater than about five times the skin depth (i.e., $d > 15 \ \mu$m at 500 MHz) can be accurately calculated using the formula (*22*)

$$R_{coil} = \frac{l\xi}{d} \sqrt{\frac{\mu_0 \rho f_0}{\pi}}. \qquad [10]$$

In this equation, ρ is the resistivity of coil wire ($\sim 1.72 \times 10^{-8} \ \Omega$ m for copper), f_0 is the resonant frequency in hertz ($\omega_0/2\pi$), and ξ is an enhancement factor that arises from the proximity of adjacent turns. Experimentally verified values of ξ are reported elsewhere as a function of (1) the coil's length-to-diameter ratio (l_{coil}/d_{coil}), (2) the number of turns (n), and (3) the ratio between the wire diameter (d) and the center–center distance (s) between adjacent turns (*22, 23*).

The SNR in Time and Frequency Domains

In principle, the SNR in the time domain is the most easily predicted since it is independent of NMR line width and shape. In the 3D-CSI experiment illustrated in Fig. 1, this important measure of NMR performance can be calculated using Eqs. [1]–[10]. When the static field strength (B_0) is 11.7 T, the spin quantum number (I) is 1/2, the noise figure (F) is 0.6 dB, and the temperature of both sample (T_s) and coil (T_{coil}) is $\sim 21°$C ($\sim 294°$K), the equations can be combined to give the following

expression:

$$\text{SNR}_t = 6.52 \times 10^{-12} \ \beta \ (t = TE) \ N \ B_{xy} \ V_{voxel} \sqrt{\frac{N_{total}}{R_{coil} \Delta f}}. \qquad [11]$$

Of course, it is often preferable to analyze a NMR spectrum and, consequently, it is also useful to determine the signal-to-noise ratio in the frequency domain (SNR_f). To generate localized NMR spectra from 3D-CSI data, the time-dependent signal $S(t)$ associated with each voxel is Fourier transformed. Equation [5] shows that the resulting absorption spectrum is Lorentzian and has a full width at half maximum (f_{FWHM}) of $(\pi T_2)^{-1}$ hertz. Therefore, if B hertz of additional Lorentzian broadening is applied, the maximum signal in the frequency domain is just $S(t = TE)/[\pi(f_{FWHM} + B)]$. Moreover, if the acquisition time (T_{acq}) is much greater than $[\pi(f_{FWHM} + B)]^{-1}$, then the RMS noise in the spectral baseline (σ_f) is just $\sigma_t/\sqrt{2\pi \Delta f B}$ (*24*). Defining the SNR in the frequency domain (SNR_f) as the peak spectral intensity divided by twice the RMS noise in the spectral baseline then gives the following formula, which is conveniently expressed in terms of the predicted SNR in the time-domain:

$$\text{SNR}_f = \text{SNR}_t \frac{\sqrt{2\pi \Delta f \ B}}{\pi(f_{FWHM} + B)}. \qquad [12]$$

MATERIALS AND METHODS

The microcoil assembly shown in Fig. 2 was used to examine projected ^{1}H NMR sensitivity at 500 MHz. The assembly itself was manufactured by Doty Scientific Inc. (Columbia, SC) and houses a 12-turn microcoil with an average length (l_{coil}) and diameter (d_{coil}) of 500 and 267 μm respectively. To reduce susceptibility variations around the sample and ensure adequate static field B_0 homogeneity, the coil is encapsulated with an epoxy having a magnetic susceptibility (χ) of roughly -11.5 ppm, which is close to the -9.6 ppm of copper. The use of encapsulation also adds rigidity to the coil structure so that the coil itself can be freestanding with no need for a former. In practice, this provides more usable space in the coil's interior and allows sealed sample tubes to be inserted or removed during routine measurements. Because the assembly was designed for research on small cell systems, its architecture is such that sample temperature can be regulated by circulating warm or cold gas, and if desired, open access to the coil bore may be sealed to flow liquid directly into the sample region through integrated plumbing.

Based on the microcoil's dimensions, the RF field strength produced at the coil center (B_{xy}) is estimated to be ~ 0.027 T/A (see Eq. [3]). The coil itself was wound with polyurethane-coated copper wire (48 AWG, $d \sim 31 \ \mu$m), and the total length of wire (l) is estimated to be ~ 0.011 m if lead length is neglected ($l = n\pi d_{coil} + l_{coil}$). Given that the center-to-center spacing
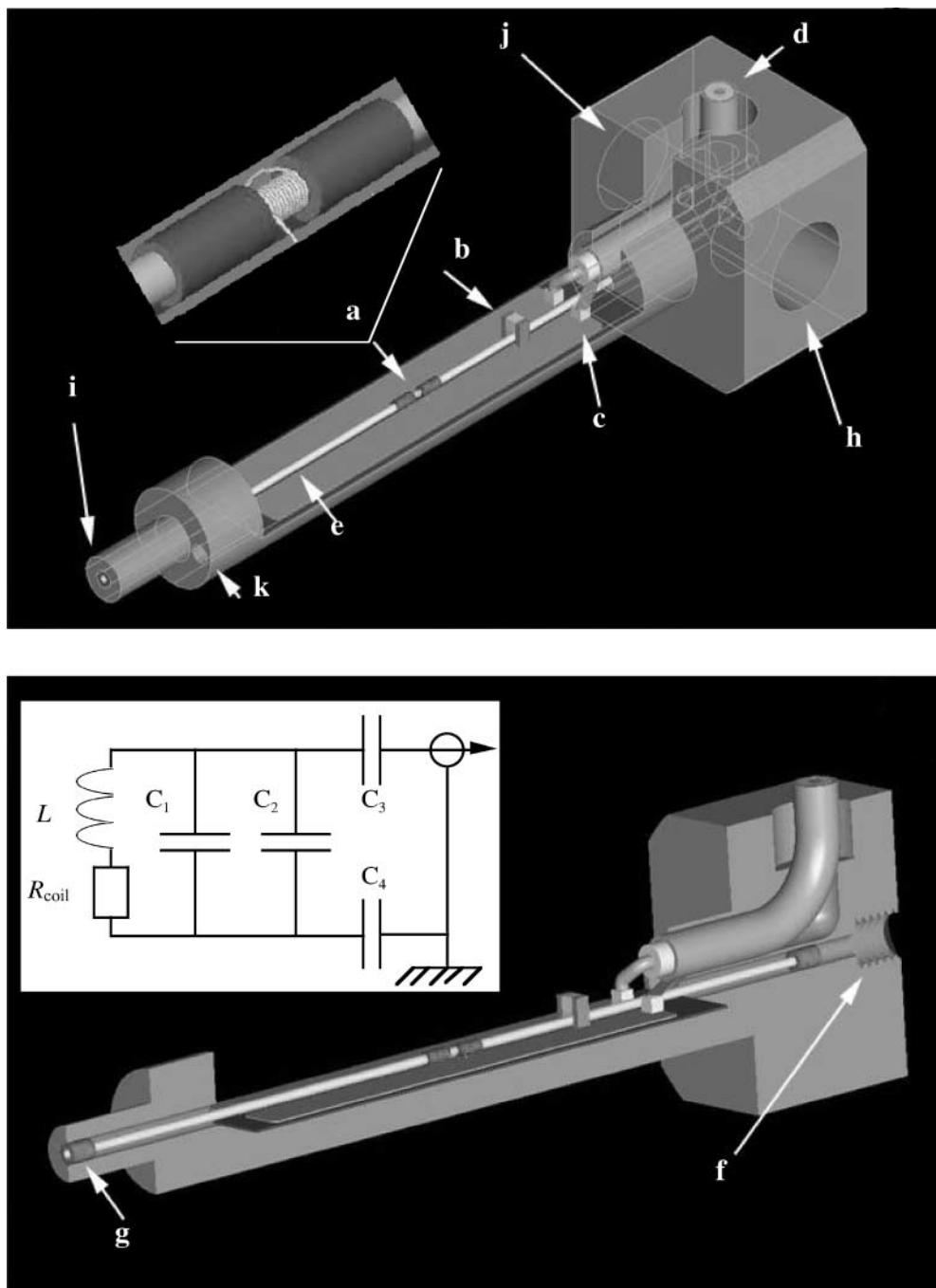
FIG. 2. (Courtesy of Doty Scientific, Inc, Columbia, SC). CAD renderings of the microcoil assembly. Insert: RF circuit diagram where L represents the microcoil's self-inductance (theoretical value $\sim$15.3 nH (22)). The microcoil is integrated into a Torlon housing for mechanical stability. The coil region (a) is shielded by a slotted layer of thin copper foil ($\sim$200 μm thick) that is glued to the outside of a shortened 5-mm NMR tube. This, in turn, slides over the elongated stem of the housing and is not shown for clarity. The overall length of the assembly is $\sim$40 mm, and the length of the cylindrical stem formed with the RF shield in place is $\sim$30 mm. (a) Microcoil and Aurum cylinders attached to each end of the coil. The space around the coil is filled with low-viscosity epoxy. The coil leads are soldered to wide, low-inductance, low-loss conductors on an Ultra-lam substrate. These conductors have a total capacitance (C1 in the insert) of $\sim$2.3 pF and provide the majority of the parallel capacitance required to tune the coil to 500 MHz. (b) 1-pF ATC chip capacitor (C2 in the insert). (c) Two 4.0-pF ATC match capacitors (C3 and C4 in the insert). (d) RF feed line, consisting of a short length of flexible 50-Ω double-shielded miniature coax with Goretex dielectric. This feed line is, in turn, connected to a 50-Ω semirigid coaxial cable to form a lambda transmission line. A remote tune/match box is then attached outside the magnet for fine adjustment of tuning and matching. (e) Polyimide tubing with an ID of 0.2 mm. (f) Clear bore access for insertion/removal of a capillary tube. Access is achieved by removing a 1-72 brass screw from the rear of the assembly. (g) Aurum collars (sealed with epoxy) around the polyimide tubing to prevent leaking if a liquid sample is flowed into the sample chamber via (h) inlet, and (i) flow-through outlet. (j) VT gas inlet. (k) VT gas outlet.

$(s = l_{\text{coil}}/n)$ between adjacent turns is $\sim 42\ \mu$m, and that $\xi \sim 2.4$ for a 12-turn coil when $l_{\text{coil}}/d_{\text{coil}} \sim 1.9$ and $d/s \sim 0.75$ (22), coil resistance (R_{coil}) at 500 MHz is estimated to be $\sim 1.5\ \Omega$ (see Eq. [10]). Based on expressions given elsewhere (22), the coil's self-inductance (L) is estimated to be ~ 15.3 nH. Consequently, the microcoil's quality factor ($Q = \omega_0 L/R_{\text{coil}}$) is estimated to be roughly 32. Interestingly, the measured Q of the tuned and matched circuit was ~ 42 and this did not change when a lossy sample was introduced. The larger circuit Q is undoubtedly related to the fact that a significant fraction of the circuit's electromagnetic energy is stored in relatively low loss structures such as the coil's leads and the transmission line—both of which can introduce significant inductance. It is this phenomenon that ultimately diminishes the utility of Q measurements as a gauge of overall circuit performance when a microcoil is employed.

Achieved SNR performance was tested at room temperature ($T_s \sim T_{\text{coil}} \sim 21°$C $\sim 294°$K) using a Varian UNITY Plus imaging spectrometer equipped with a standard 89-mm vertical bore magnet operating at 11.7 T (B_0). Prior to the measurements, the noise figure F of the receiver was measured to be ~ 0.6dB using a calibrated noise source and a procedure described elsewhere (25). To perform 3D-CSI, the entire assembly shown in Fig. 2 was mounted inside a horizontal-bore gradient package manufactured by D. G. Cory and co-workers at MIT. With 30 A of current, this was capable of producing 2.5 T/m along the bore axis, or 10 T/m along each orthogonal axis (26).

In order to assess the utility of the RF probe for cellular research, sensitivity measurements were performed using distilled water doped with 6.6 mM $CuCl_2$ and 33 mM choline chloride (Aldrich Chemical Company). The former was added to shorten T_1's, and the choline concentration used is similar to that measured in live mammalian cells (6). Measurements were also performed using a single globule excised from the ovary of a young female *Xenopus laevis* frog. Depending on the age of the frog, ovaries can contain oocytes at different stages of oogenesis. These amphibian cells are large, are spherical in shape, and have diameters ranging from $\sim 200\ \mu$m in stage 1 to ~ 1.3 mm in stage 6 (27). The ovaries in young frogs also contain thousands of 100-μm-diameter transparent globules that, unlike stage-1 oocytes, float in Barth's medium, do not stain for DNA, and do not contain a germinal vesicle or Balbiani bodies. At present, it is unknown whether these globules are oocyte precursors or merely serve another function such as providing a surface for future follicle cell attachment.

Prior to ^{1}H NMR experiments, each sample was first loaded into a silica capillary having an outer diameter of 200 μm and an inner diameter of 100 μm (Polymicro Technologies, Phoenix, AZ). After open ends were sealed using 5-min epoxy, the capillary was then loaded into the clear bore of the microcoil assembly (see Fig. 2). The static field was then shimmed and each sample's relaxation properties were measured using techniques employed in previous work (6).

RESULTS

In experiments performed using the doped water sample, the signal-to-noise ratio in the time domain (SNR_t) was largely determined by water protons since choline was only present in trace amounts. In bulk water where $n_s = 2$ and C is ~ 55.4 M at room temperature, the spin density N predicted by Eq. [8] is approximately 6.67×10^{28} protons per cubic meter, and the thermal equilibrium magnetization (M_0) predicted by Eq. [7] is about 0.038 A/m at 11.7 T. Measured values for water's T_1, T_2, and diffusion coefficient (D) were 0.37 s, 0.24 s, and 2.0×10^{-9} m^2/s respectively.

To test expressions used for predicting the time domain signal-to-noise ratio (SNR_t), a 200-μm-thick slice was selected at the center of the microcoil and the pulse sequence illustrated in Fig. 1 was used to image the capillary's cross-section. Raw CSI data was collected using two averages and eight phase-encoding steps along each orthogonal direction—for a total (N_{total}) of 128 acquisitions. The field of view (FOV) was 128 by 128 μm, and the planar resolution was therefore $16 \times 16\ \mu$m. Consequently, the volume associated with each voxel (V_{voxel}) was $\sim 51.2 \times 10^{-15}$ m^3 or about 51 pL. Raw CSI data were acquired using a bandwidth (Δf) of 8400 Hz, an acquisition time T_{ACQ} of 1.0 s, a TE of 0.008 s, and a TR of 1.2 s. In addition, the slice-select gradient strength (G_{slice}) was 0.87 T/m, and $t1$–$t5$ were 0.0003, 17×10^{-6}, 0.0019, 483×10^{-6}, and 0.0013 s respectively (cf. Fig. 1). Under these conditions, b_{slice} is predicted to be 83×10^6 s/m^2, $\beta(t = \text{TE})$ is ~ 0.79, and the theoretical value of SNR_t calculated for water using Eq. [11] is therefore ~ 46. This is comparable to the experimental value of 32 ± 2 measured using localized time-domain signals in the selected slice.

Spectroscopic detection limits were examined using the choline ^{1}H NMR signal measured in a second CSI experiment performed using the same doped water sample. Unlike in the first, however, water saturation was employed to ensure its ^{1}H NMR signal would not distort the spectral baseline in the vicinity of choline's relatively small peaks. In practice, these reside at 3.2 ppm $(CH_3)_3$, 3.6 ppm (N–CH_2), and 4.2 ppm (O–CH_2). The largest of these—at 3.2 ppm—arises from choline's nine methyl protons ($n_s = 9$). With a choline concentration of 33 mM, these are predicted to have a spin density N of roughly 1.79×10^{26} protons per cubic meter—which is nearly 400 times lower than that of water. Measured values for the methyl peak's T_1, T_2, and diffusion coefficient (D) were 1.8 s, 0.5 s, and 1.0×10^{-9} m^2/s respectively. Because of choline's longer T_1, the TR was increased to 2.5 s, and the loss factor β $(t = \text{TE})$ was therefore ~ 0.68. In addition, 64 averages were used instead of 2 to improve SNR performance. Consequently, N_{total} was 4096. All other acquisition parameters were identical to those used in the first CSI experiment already described.

Figure 3A shows the localized ^{1}H NMR spectrum acquired from a single voxel having a volume of 51 pL. The applied line broadening (B) was 20 Hz and the measured linewidth of the
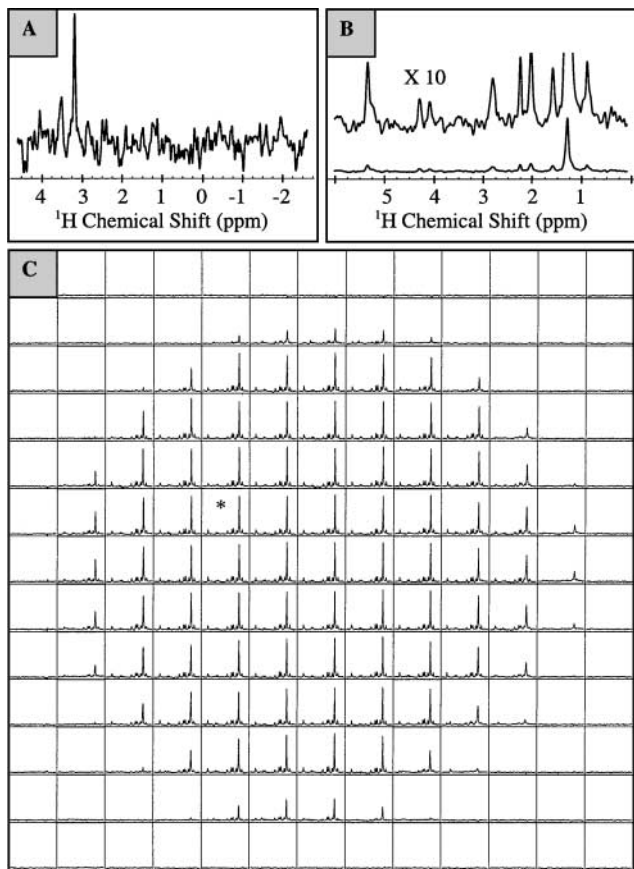
FIG. 3. (A) Localized ¹H NMR spectrum acquired from 51.2 pL of distilled water doped with 33 mM choline chloride. The spectrum shows choline's methyl line at 3.2 ppm. It was generated from CSI data using the processing and acquisition parameters described in the text. (B) Localized ¹H NMR spectrum acquired from a 5-pL voxel inside a 100-μm-diameter globule excised from the ovaries of a young *Xenopus laevis* frog. The spectrum is part of the CSI data set shown in (C). There, the spectrum for each voxel in a 50-μm-thick slice centered on the globule is shown, and an asterisk denotes the location of the voxel used for (B). Raw data were generated using 32 averages and 16 phase-encoding steps per axis—for a total (N_{total}) of 8192 acquisitions. Other parameters included a TE of 0.008 s, a TR of 0.3 s, and an acquisition bandwidth (Δf) of 11,200 Hz. Since the diffusion coefficient was almost a hundred times smaller than that for bulk water, diffusion losses could be neglected and β ($t =$ TE) is predicted to be ~0.38. Each globule spectrum was generated using 10-Hz line broadening (B) and the average measured line width ($B + f_{FWHM}$) for the methylene peak at 1.3 ppm is about 30 Hz.

broadened methyl peak ($f_{FWHM} + B$) is roughly 37 Hz. Because of the low SNR, choline's other two peaks are not observed, since only two protons per molecule contribute to each. Given the amount of applied line broadening (B) and the measured line width ($B + f_{FWHM}$), Eq. [12] predicts a signal-to-noise ratio in the frequency domain (SNR_f) of 5.4. This was close to the average value of 4.4 ± 0.9 measured from voxels within the selected slice.

Figure 3B shows the localized ¹H NMR spectrum acquired from a single voxel inside the *Xenopus* globule. The voxel, and its associated spectrum, is part of the larger CSI data set shown

in Fig. 3C. There, CSI data from a 50-μm-thick slice through the globule's cross section are shown with a 10×10-μm planar resolution. Each voxel, therefore, only contains 5 pL of sample.

The similarity of spectra in different voxels shown in Fig. 3C suggests that the globule's chemical composition is homogeneous. Each spectrum reveals that the tissue contains no water and is composed only of triacylglycerols (TAGs) (*28, 29*). This is in contrast to spectra obtained from stage 2 and larger oocytes where water, lipids, and other metabolites are observed (*30–32*). Analysis of acquired spectra shows that the fatty acids attached to the glycerol esters have an average chain length of roughly 19 carbons, including approximately 10 methylene (CH₂) groups that contribute to the peak at 1.3 ppm, and 2 olefenic groups—giving an average molecular weight of ~980. Consequently, if the globule is completely filled with TAGs, and their specific density is assumed to be ~0.94 g/ml, which is that of most oils composed of TAGs (e.g., olive and cottonseed (*33, 34*)), then their molar concentration (C) is predicted to be about 0.96 M.

To facilitate a comparison between predicted and measured SNR performance, the diffusion coefficient (D), T_1, and T_2 of methylene protons were measured to be 1.5×10^{-11} m²/s, 0.59 s, and 0.16 s, respectively. Together with the acquisition parameters given in the caption of Fig. 3B and the estimate that each TAG contains ~60 methylene protons (n_s), a SNR_f of about 72 is predicted for the methylene line at 1.3 ppm. This is somewhat higher than the measured value of 57 ± 6 but still in excellent agreement with observed performance.

DISCUSSION

In earlier work, the measured signal-to-noise ratio in the time domain (SNR_t) was shown to agree closely with theoretical values expected in bulk ¹H NMR experiments conducted at 200 MHz with microcoils wound with diameters as small as 50 μm (*1*). In this study, close agreement between theory and measured SNRs in both time and frequency domains was demonstrated at 500 MHz in spectroscopic imaging experiments performed with a 267-μm-diameter microcoil. It was also shown that achieved ¹H NMR sensitivity is often sufficient for resolving picoliter-scale sample volumes, particularly when detected compounds have concentrations typically found in biological cells and tissues.

In the current study, the minimum number of chemically equivalent protons (NV_{voxel}) detected was the approximately 10^{13} methyl protons that contributed to the observed peak at 3.2 ppm in Fig. 3A. Given the spectrum's low SNR_f (4.4), this may be assumed to be the minimum detection limit achievable under the specified experimental conditions. Interestingly, this is the same number of protons in roughly 0.15 pL of bulk water. Consequently, one might expect to resolve a comparable volume in a water imaging experiment. This projection is in qualitative agreement with the 0.2 pL-resolution that was recently

reported at 600 MHz in experiments performed using slightly more scans (16,384) and a somewhat larger 740-μm-diameter microcoil (2).

In this study, experimental data was acquired using a unique microcoil housing that provided sufficient mechanical strength for routine measurements. However, because the measured linewidth (f_{FWHM}) for the methyl–choline peak was ~17 Hz, and the theoretical limit $(\pi T_2)^{-1}$ is less than one, spectral sensitivity was not optimal (see Eq. [12]). It is likely that this residual broadening is attributable to susceptibility differences between the various components of the microcoil assembly since considerably narrower lines were obtained with the same gradient coil package using much larger solenoids having less material in close proximity to the sample (e.g., capacitors, tubing, glue). Susceptibility-induced broadening also likely explains why the ability to shim varied with the probe's orientation in the gradient bore and the fact that in some cases, strong dc shim gradients (~50 mT/m) generated with the gradient coil package needed to be employed. Despite these shortcomings, however, achieved static field homogeneity was sufficient for cellular research where the linewidths are often considerably larger (6) than the observed degree of residual broadening reported here.

The work presented in this study illustrates the effectiveness of using a small, room-temperature NMR receiver coil to increase the SNR achieved per unit sample volume in studies involving small biological samples. Of course, an alternative method that can be exploited to achieve the same outcome is to cool the NMR coil, its RF circuitry, and the receiver (4). In this context, it is useful to consider whether or not a cold probe could be used to achieve the same SNR performance reported here. As a specific example, we limit our discussion to the so-called cryogenic probes that are becomingly increasingly popular for NMR spectroscopy. Although these normally contain cooled copper coils, their SNR performance is comparable to that achieved with a probe containing a high-temperature superconducting receiver coil. In this context, the considerations are largely applicable to a cold probe containing either type of coil.

In a well-designed cryogenic probe, a 5-mm-diameter copper coil typically operates at 25 K, and the cryostat is small enough to accommodate a 3-mm OD sample tube that is maintained at room temperature. In ^{1}H NMR studies performed at 500 MHz with a probe of this type, the SNR is increased by roughly a factor of 3 over an otherwise identical room-temperature probe—when sample losses can be neglected [35]. In a cold probe, however, a 1-mm spacing between the coil and the sample tube is necessary to vacuum isolate the sample from the coil and its associated cooling system. We assume that this same distance would also be needed when smaller samples are used. Therefore, in the current study, where the sample tube had a 200-μm OD, the smallest possible coil diameter that could be used in a cryogenic probe would be about 2.2 mm rather than 267 μm. As the SNR is approximately inversely proportional to the coil diameter (see below), this means that the increase in the coil diameter dictated by

the need to accommodate a cryostat causes a decrease in the SNR by roughly a factor of 8—which is only partially compensated for by the factor of 3 gained by cooling the probe. When room-temperature coils with diameters of less than a millimeter can be employed, this example illustrates that it is unlikely that cooled probes can be used to achieve the same SNR performance unless significant advances are made in reducing the size of the required cryostat.

In light of the above considerations, it is perhaps useful to speculate about what type of SNR performance might be achievable if coil dimensions in a room temperature NMR probe were further reduced and issues regarding fabrication and static field homogeneity could be ignored. Of course, the answer depends strongly on the various factors affecting the SNR. Therefore, as a specific example, we consider the case where one wants to perform ^{1}H NMR spectroscopy at 500 MHz on biological cells containing ~33 mM choline using the same acquisition parameters (i.e., Δf, N_{total}, etc.) employed for the choline measurements already described. It is further assumed that relaxation losses can be neglected and both the coil's length-to-diameter ratio (l_{coil}/d_{coil}) and the ratio between its wire diameter (d) and wire spacing (s) remain constant as dimensions are reduced. In this case, the equations presented here and elsewhere show that the SNR varies directly with the volume of each voxel (V_{voxel}) and inversely with coil diameter (d_{coil}) when the wire diameter is greater than about 5 times the skin-depth (i.e., $d > 15$ μm at 500 MHz) (1).

Based on this simple scaling relationship (i.e., SNR $\propto V_{voxel}/d_{coil}$), maximum sensitivity will be achieved with a small coil by completely filling it with sample so that V_{voxel} is approximately equal to the coil volume, and V_{voxel}/d_{coil} is therefore ~$0.25\pi d_{coil}^2 (l_{coil}/d_{coil})$. Equating this expression to the same ratio in the current study (i.e., $V_{voxel}/d_{coil} \sim 1.9 \times 10^{-10}$ m^2) then suggests that an SNR$_f$ of ~4.4 might be achievable if the coil diameter (d_{coil}) were reduced to ~11 μm and data were acquired from ~2 pL of sample. Remarkably, this is roughly the same volume of a single mammalian cell assuming an average cell diameter of ~15 μm. Moreover, if it were indeed possible to fabricate such a small coil and achieve theoretical SNR performance, it might also be possible to obtain water images with the same SNR (4.4) using voxels containing only ~9×10^{-18} m^3 of sample (roughly 2 μm isotropic resolution), particularly if an average intracellular water concentration of 30 M (6) is assumed. In combination with strong gradients to minimize T_2 and diffusion losses, subcellular spatial resolution in water images might then be achieved together with single-cell ^{1}H NMR spectroscopy.

Of course the example just described is oversimplified and achieving such dramatic SNR performance will undoubtedly be technically challenging. Furthermore, since wire thinner than 15 μm would ultimately be needed to wind such a small coil, the skin-depth limit upon which the calculation is based is not strictly satisfied and the SNR then varies with $\sim \sqrt{d_{coil}^{-1}}$ at very small coil dimensions (1). Nevertheless, using the data given

in Ref. (*1*), it can be shown that this hardly changes the outcome and the small reduction in anticipated sensitivity due to the use of wire thinner than 15 μm, would likely be compensated for, for example, by doubling the number of acquisitions (N_{total}). It is in this context then, together with ongoing advances in microcoil fabrication, that such prospects may not be far off.

ACKNOWLEDGEMENTS

REFERENCES

1. T. L. Peck, R. L. Magin, and P. C. Lauterbur, Design and analysis of microcoils for NMR microscopy, *J. Magn. Reson. Ser. B* **108,** 114–124 (1995).

2. S. C. Lee, K. Kim, J. Kim, S. Lee, J. H. Yi, S. W. Kim, K. Ha, and C. Cheong, One micrometer resolution NMR microscopy, *J. Magn. Reson.* **150,** 207–213 (2001).

3. S. Choi, X.-W. Tang, and D. G. Cory, Constant time imaging approaches to NMR microscopy, *Int. J. Imaging Systems Technol.* **8,** 253–276 (1998).

4. E. W. McFarland and A. Mortara, Three-dimensional NMR microscopy: Improving SNR with temperature and microcoils, *Magn. Reson. Imaging* **10,** 279–288 (1992).

5. D. L. Olson, T. L. Peck, A. G. Webb, R. L. Magin, and J. V. Sweedler, High-resolution microcoil 1H-NMR for mass-limited, nanoliter-volume samples, *Science* **270,** 1967–1970 (1995).

6. K. R. Minard, X. Guo, and R. A. Wind, Quantitative 1H MRI and MRS microscopy of individual V79 lung tumor spheroids, *J. Magn. Reson.* **133,** 368–373 (1998).

7. S. C. Grant, N. R. Aiken, H. D. Plant, S. G. Gibbs, T. H. Mareci, A. G. Webb, and J. Blackband, NMR spectroscopy of single neurons, *Magn. Reson. Med.* **44,** 19–22 (2000).

8. R. Pohmann, M. von Kienlin, and A. Haase, Theoretical evaluation and comparison of fast chemical shift imaging methods, *J. Magn. Reson.* **129,** 145–160 (1997).

9. T. R. Brown, B. M. Kincaid, and K. Ugurbil, NMR chemical shift imaging in three dimensions, *Proc. Natl. Acad. Sci. USA* **79,** 3523–3526 (1982).

10. T. H. Mareci and H. Ralph Brooker, Essential considerations for spectral localization using indirect gradient encoding of spatial information, *J. Magn. Reson.* **92,** 229–246 (1991).

11. D. I. Hoult and R. E. Richards, The signal-to-noise ratio of the nuclear magnetic resonance experiment, *J. Magn. Reson.* **24,** 71–85 (1976).

12. D. I. Hoult, The principle of reciprocity in signal strength calculations—A mathematical guide, *Concepts Magn. Reson.* **12,** 173–187 (2000).

13. C.-N. Chen and D. I. Hoult, "Biomedical Magnetic Resonance Technology," Institute of Physics Publishing, Bristol, 1989.

14. C. Mahony, L. K. Forbes, S. Crozier, and D. M. Doddrell, A novel approach to the calculation of RF magnetic and electric fields for NMR coils of arbitrary geometry, *J. Magn. Reson. Ser. B* **107,** 145–151 (1995).

15. G. H. Glover, C. E. Hayes, N. J. Pelc, W. A. Edelstein, O. M. Mueller, H. R. Hart, C. J. Hardy, M. O'Donnell, and W. D. Barber, Comparison of linear and circular polarization for magnetic resonance imaging, *J. Magn. Reson.* **64,** 255–270 (1985).

16. D. I. Hoult and M. D. Phil, Sensitivity and power deposition in a high-field imaging experiment, *J. Magn. Reson. Imaging* **12,** 46–67 (2000).

17. K. R. Minard and R. A Wind, Solenoidal microcoil design. I. Optimizing RF homogeneity and coil dimensions, *Concepts Magn. Reson.* **13,** 128–142 (2001).

18. P. T. Callaghan, "Principles of NMR Microscopy," Clarendon, Oxford (1993).

19. R. R. Ernst, G. Bodenhausen, and A. Wokaun, "Principles of NMR in One and Two Dimensions," Clarendon, Oxford (1994).

20. M. Brandl and A. Haase, Molecular diffusion in NMR microscopy, *J. Magn. Reson. Ser. B* **103,** 162–167 (1994).

21. Z. H. Cho, C. B. Ahn, S. C. Juh, H. K. Lee, R. E. Jacobs, S. Lee, J. H. Yi, and J. M. Jo, Nuclear magnetic resonance microscopy with 4-μm resolution: Theoretical study and experimental results, *Med. Phys.* **15,** 815–824 (1988).

22. K. R. Minard and R. A. Wind, Solenoidal microcoil design. II. Optimizing winding parameters for maximum signal-to-noise performance, *Concepts Magn. Reson.* **13,** 190–210 (2001).

23. R. G. Medhurst, H.F. resistance and self-capacitance of single-layer solenoids, *Wireless Eng.* **24,** 35–43, 80–92 (1947).

24. D. I. Hoult, Sensitivity of the NMR Experiment, *in* "Encyclopedia of NMR" (D. M. Grant and R. K. Harris, Eds.), Vol. 7, pp. 4256–4266, Wiley, Chichester (1996).

25. D. R. Straw (Ed.), "The ARRL Handbook for Radio Amateurs," 76th ed., The American Radio Relay League, Newington, CT (1998).

26. S. Choi, X.-W. Tang, and D. G. Cory, Constant time imaging approaches to NMR microscopy, *Int. J. Imaging Systems Technol.* **8,** 263–276 (1997).

27. B. K. Kay and H. B. Peng (Eds.), "*Xenopus laevis*: Practical Uses in Cell and Molecular Biology," Methods in Cell Biology, Vol. **36,** Academic Press, San Diego (1991).

28. F. D. Gunstone, High-resolution ^{1}H and ^{13}C NMR, *in* "Lipid Analysis. A Practical Approach" (R. J. Hamilton and S. Hamilton, Eds.), pp. 243–262, IRL Press, Oxford (1992).

29. A. Kuesel, G. R. Sutherland, W. Halliday, and I. C. P. Smith, ^{1}H MRS of high grade astrocytomas: Mobile lipid accumulation in necrotic tissue, *NMR Biomed.* **7,** 149–155 (1994).

30. S. Pauser, A. Zshunke, A. Khuen, and K. Keller, Estimation of water content and water mobility in the nucleus and cytoplasm of *Xenopus laevis* oocytes by NMR microscopy, *Magn. Reson. Imaging* **13,** 269–276 (1995).

31. S. Posse and W. P. Aue, ^{1}H spectroscopic imaging at high spatial resolution, *NMR Biomed.* **2,** 234–239 (1989).

32. R. E. Jacobs and S. E. Fraser, Magnetic resonance microscopy of embryonic cell lineages and movements, *Science* **263,** 681–684 (1994).

33. R. T. Morrison and R. N. Boyd, "Organic Chemistry," 3rd ed., p-1056, Allyn & Bacon, Boston (1980).

34. R. C. Weast (Ed.), "CRC Handbook of Chemistry and Physics," 61st ed., p. F3 CRC Press, Boca Raton, FL (1980).

35. D. J. Russell, C. E. Hadden, G. E. Martin, A. A. Gibson, A. P. Zens, and J. L. Carolan, A comparison of inverse-detected heteronuclear NMR performance: Conventional vs cryogenic microprobe performance, *J. Nat. Prod.* **63**(8), 1047–1049 (2000).